UNIVERSIDAD INDUSTRIAL DE SANTANDER

TRABAJO DE GRADO

Inversión gravimétrica 3D con inicialización adaptativa y regularización secuencial: Un caso de estudio del Área Geotérmica de Cerro Machín

Director:
Yesid Paul Goyes Peñafiel

Autor:
Gabriel Moreno Sánchez

Codirector:
Sait Khurama Velasquez

Trabajo de grado para optar por el título de Geólogo

Universidad Industrial de Santander
Facultad de Ingenierías Fisicoquímicas
Escuela de Geología
Bucaramanga
2025

Inversión gravimétrica 3D con inicialización adaptativa y regularización secuencial: Un caso de estudio del Área Geotérmica de Cerro Machín

RESUMEN

La caracterización geofísica de áreas con potencial geotérmico mediante el análisis de anomalías en los datos y la inversión gravimétrica se enfrenta a retos importantes. La limitada información espacial sobre las estructuras subterráneas, combinada con los métodos convencionales que emplean la regularización de la norma ℓ_2, a menudo produce modelos de densidad con límites suavizados o difusos. Esto complica aún más la interpretación geológica y también conduce a la convergencia de cuerpos geológicamente sin sentido que se ajustan a los datos, lo que puede ocultar la verdadera naturaleza de las características geológicas. Para superar esto, presentamos un esquema de inversión gravitacional en 3D para el área geotérmica de Cerro Machín, Colombia. La metodología que proponemos integra conocimientos geológicos (límites físicos de densidad y rasgos regionales identificados en estudios anteriores) a priori para construir modelos iniciales robustos, lo que guía el proceso de inversión iterativo hacia un espacio de soluciones geológicamente plausible. Esto se complementa con una estrategia de regularización secuencial que aprovecha las normas ℓ_p para promover la delineación de cuerpos compactos y lisos con límites nítidos y no difusos en profundidad. En este trabajo, demostramos que el enfoque de doble paso —utilizando un modelo inicial restringido y la regularización de la norma ℓ_p— mejora significativamente la eficiencia y la precisión de la convergencia del modelo, a diferencia de los métodos tradicionales que se basan en la regularización de la norma ℓ_2 y en modelos iniciales homogéneos. Los resultados demuestran la eficacia de un método que combina la recuperación de estructuras subterráneas compactas en el subsuelo con la estimación de cuerpos suavizados y poco profundos, superando los enfoques convencionales al presentar soluciones geológicamente razonables en un proceso eficiente que implica modelos iniciales. Esto proporciona un marco de inversión adecuado para la exploración geotérmica en sistemas volcánicos análogos. El código está disponible en: https://github.com/GabrielMoreno09/3DGravityInversionCMGA.git

Palabras clave: inversión 3D, gravimetría, área geotérmica, modelos iniciales, regularización, norma ℓ_p.

OBJETIVOS

Objetivo general

Desarrollar una metodología de inversión gravimétrica tridimensional basada en regularización secuencial y en la construcción de modelos iniciales guiados por información geológica y geofísica a priori, con el fin de obtener un modelo cuantitativo de densidad que permita delimitar e interpretar los elementos prospectivos del sistema geotérmico del Área Geotérmica de Cerro Machín.

Objetivos específicos

1. Construir modelos iniciales adaptativos basados en la integración de información geológica a priori y el análisis de la distribución espacial de la anomalía gravitacional residual del AGCM.

2. Diseñar e implementar un algoritmo para la inversión geofísica tridimensional de datos gravimétricos mediante esquemas de regularización secuencial ("*smooth*" y "*blocky*").

3. Validar y evaluar cuantitativamente el modelo invertido, interpretando su coherencia geológica a partir de la comparación con estudios previos.

PREGUNTA DE INVESTIGACIÓN

¿Cómo el análisis de información geológica a priori contribuye al desarrollo de metodologías de inversión gravimétrica para la generación de modelos conceptuales y tridimensionales que representen los elementos prospectivos del Área Geotérmica de Cerro Machín?

3D Gravity Inversion with Adaptive Initialization and Sequential Regularization: A case study in Cerro Machín Geothermal Area

ABSTRACT

Conventional 3D gravity inversion with ℓ_2 regularization tends to blur density contrasts in diffuse bodies, complicating interpretation in volcanic and geothermal areas. We present a two-stage inversion for the Cerro Machín Geothermal Area (Colombia) that focuses on compact structures with well-defined boundaries at depth, while preserving smooth trends at shallow depths. Stage 1 uses ℓ_2-norm regularization to obtain a stable and smooth model. Stage 2 starts from the model recovered in the first stage, which is injected as a starting model with geological *a priori* information that includes a body determined from the analysis of the width of the anomalies and regional geology, and applies a mixed norm formulation ℓ_p-norm in the model, to promote compactness and sharp interfaces. A conservative continuation strategy (robust uncertainties per data point, modest normalized depth weighting, β cooling, and backtracking) keeps updates localized, so that deviations from the starting model are based on the data. Compared to ℓ_2 inversions from starting homogeneous models, our results show the sequential approach achieves comparable mismatch with sharper boundaries, deeper compact bodies, and greater edge fidelity, achieving convergence of geological results in less time and iterations thanks to the implementation of starting models that place us at a local minimum and collaborate to reach the global minimum. Stability checks based on perturbations of the starting model and spatial cross-validation indicate that the recovered deep anomalies persist under reasonable changes in noise and hyperparameters. This workflow offers a practical framework for delineating geothermal targets using gravity-based methods in analogous volcanic systems. Code is available at: https://github.com/GabrielMoreno09/3DGravityInversionCMGA.git

INTRODUCTION

In the global transition toward a sustainable energy model, geothermal energy has emerged as a strategic resource due to its versatility and high potential for industrial application (Alfaro et al., 2021). Despite promising prospects, many geothermal areas in Colombia lack a comprehensive three-dimensional conceptual model of the subsurface density structures, which would facilitate an understanding of the relationships between their components (Nigussie et al., 2023). The Cerro Machín Geothermal Area (CMGA), stands out as a promising, active volcanic-geothermal system whose internal structural characterization remains a significant research opportunity (Morales et al., 2021). Geophysics, particularly gravimetry, provides an indispensable tool for delineating these deep structures on a regional scale (Kearey et al., 2013). However, the accurate estimation of these systems requires advanced three-dimensional (3D) gravitational inversion methodologies that can recover compact bodies with well-defined boundaries (Miller and Williams-Jones, 2016) and integrate *a priori* geological knowledge to ensure geologically coherent solutions. Tarantola (1984) defines *a priori* geological knowledge as any knowledge independent of gravimetric data that is incorporated into the inversion to define initial conditions.

The geophysical characterization of areas with potential for geothermal exploration has traditionally relied on gravity anomaly analysis (Telford et al., 1990) which identifies mass deficits and surpluses in the subsurface but provides limited constraints on the geometry or depth of causative bodies. The Mean Anomaly Width Method (MAWM), developed by Dobrin and Savit (1960), is commonly used in forward modeling to estimate structure depths based on anomaly interpretation. More advanced strategies emerged with Li and Oldenburg (1998), who introduced a 3D inversion framework that minimizes a model objective function while allowing for the incorporation of *a priori* information, thereby producing models that are both data-fitting and geologically reasonable. Subsequently, geophysical information with physical constraints was implemented to addresses the inversion to reasonable models (Fernando et al., 2007; Uieda and Barbosa, 2012; Yin et al., 2024), although, Blaikie et al. (2014) and Miller et al. (2022) improved this paradigm, demonstrating the utility of reference models that incorporate geological information to guide convergence. Peng and Liu (2021) integrated adaptive ℓ_p-norm regularization, in contrast to conventional methods that use ℓ_2-norm regularization, to enhance the estimation of compact bodies with sharp, non-diffuse boundaries. Witter et al. (2016) emphasized the benefits and potential difficulties of intro-

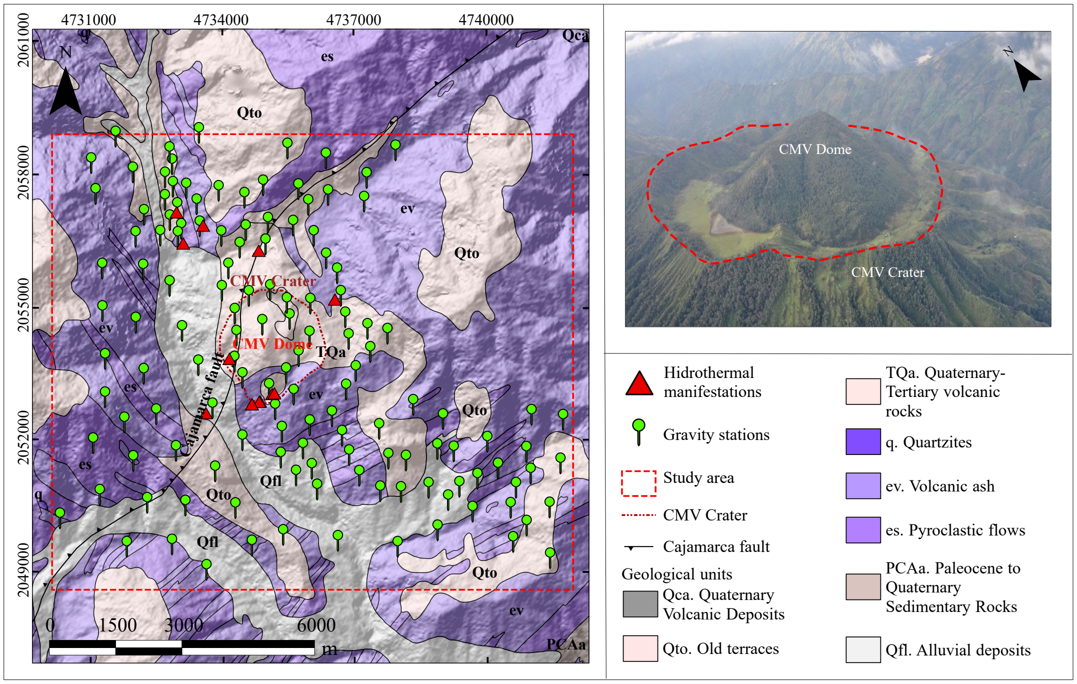

Figure 1: Location and geological map of the CMGA study area showing geophysical survey gravity stations from Beltrán (2020) with green pins. It has a MAGNA-SIRGAS coordinate system (National Geocentric Reference Frame), key volcanic features include the Cerro Machín Volcano crater and volcanic dome, overlaid on the geological base map modified from Mosquera et al. (1982) (1982, Plancha 244 – Ibagué, scale 1:100000). The inset aerial photograph of the CMV dome and crater was adapted from El Espectador (2024).

ducing geological constraints in gravity inversion, warning against over-restriction of homogeneous assumptions. A key advance was presented by Fournier and Oldenburg (2019), who provided a rigorous mathematical framework for ℓ_p-norms where p is a continuous parameter within $0 \leq p \leq 2$, with $p = 2$ producing smooth models, $p = 1$ promoting sparsity, and $p = 0$ yielding compact focused structures, linking their features as guidelines for convergence to a compact bodies. Crucially, they highlighted that in non-convex inversion problems, geologically plausible solutions are most effectively obtained when the inversion is initialized with a geologically meaningful starting model.

Despite multiple methodological approaches to 3D gravity inversion, a significant challenge remains in estimating compact and deep structures that retain geological meaning. The inherent ill-posedness of the inverse problem, traditionally mitigated by ℓ_2-norm smoothness constraints, tends to produce models with diffuse boundaries that are geologically ambiguous (Li and Oldenburg, 1998; Oldenburg and Li, 2005). To address this, some studies have explored the use of *a priori* information. For example, Foss (2005) demonstrated that using a parametric inversion result as a starting model can guide a voxel-based inversion toward a geologically constrained solution, even with the limitations of the ℓ_2-norm. However, injecting such information into reference models can bias the algorithm's search space, potentially limiting the solution rather than guiding it and leading to convergence on geologically false local minima (Farquharson et al., 2008; Blaikie et al., 2014; Miller et al., 2022; Ghalenoei et al., 2022). Alternatively, regularization strategies have been developed to promote sparsity and image focusing (Routh et al., 2007; Sacchi and Liu, 2005). These methodologies implement ℓ_p-norms ($0 \leq p \leq 2$) to counteract the tendency of ℓ_2 regularization to produce smooth and dispersed models, thus promoting the recovery of compact geological bodies with sharp boundaries (Sun and Li, 2014; Miller et al., 2017; Trevino et al., 2021; Zhu et al., 2024). To ensure the recovery of geologically plausible structures, deterministic optimizations are implemented to guide the solution towards a local minimum that approximates the global minimum (Lelièvre and Oldenburg, 2009; Guillen et al., 2008). In this context, Rashidifard et al. (2024) presents an innovative methodology for non-convex inversion problems that uses starting models to guide the inversion toward a local minimum of significant geological relevance, rather than imposing restrictive constraints that can bias the solution.

In this work, we address these limitations by developing a three-dimensional gravitational inversion model for two-phase flow, adapted to the CMGA in Colombia. Our approach combines an starting model with geological information —constructed from the MAWM and regional *a priori* geological information— with a sequential and adaptive regularization scheme to recover compact bodies with well-defined boundaries at depth, while preserving the smooth trends of shallow structures. In the first stage, we use a Weighted Least Squares (WLS) inversion with ℓ_2 norm regularization to recover a stable and smoothed model. In the second stage, this smoothed model is used for a mixed ℓ_p norm Iterative Reweighted Least Squares (IRLS) inversion to promote compactness and edge delineation (Li and Oldenburg, 1998; Sun and Li, 2014; Fournier and Oldenburg, 2019; Peng and Liu, 2021). The proposed framework, accompanied by a conservative iteration step strategy (standard deviation per data point σ, modest depth weighting, fast cooling β, and backtracking search within a Projected Gauss-Newton-Conjugate Gradient framework) keeps updates localized. Compared to conventional inversion methodologies with ℓ_2 norm regularization initialized from homogeneous or random models, known for blurring edges, our method achieves an objective mismatch that converges large-scale bodies with high density contrast, compact and deep with sharp boundaries and geological meaning in fewer iterations and less time than other methodologies (Blaikie et al., 2014; Miller et al., 2022). The result moves us away from biased interpretations and provides a comprehensive three-dimensional view of the constituent elements of the CMGA, enabling its spatial, morphological, and volumetric characterization. Although developed for the CMGA, the methodological framework constitutes a transferable strategy for imaging compact geothermal targets in analogous volcanic systems.

GEOLOGICAL AND GEOPHYSICAL BACKGROUND

The CMGA is situated in the Central Cordillera of Colombia (EPSG 9377: 4.28°N, 75.24°W), representing one of the most significant active volcanic systems with substantial geothermal potential in the country (Gutiérrez, 2020). Figure 1 shows the entire geothermal area with a volcanic crater of 2.4 km in diameter which containing multiple dacitic domes that were emplaced within a basement of metamorphic rocks and volcanoclastic deposits (Pedraza et al., 2022). The volcano's explosive history includes at least six significant eruptions in the last 5000 years, with the most recent significant event occurring approximately 800 years ago, making it a critical hazard and an energetic resource of interest (Herrera and Calò, 2025). Gutiérrez (2020) compile Petrographic and field information that indicate that the dome consists predominantly of dacitic lavas and pyroclastic flows, with secondary argillic alteration near fumarolic zones. The Cajamarca fault, characterized by Mosquera et al. (1982) defines a high-fracture zone that acts as the main conduit for ascending geothermal fluids, while permeable pyroclastic and terrace deposits on the flanks serve as recharge pathways.

Beltrán (2020) identified significant anomalies associated with the Cerro Machín Volcano (CMV) and its adjacent NW and SE sectors using gravimetric and magnetometric geophysical surveys. Figure 2 shows the spatial distribution of the residual gravity anomaly, illustrating a prominent low-gravity zone (blue zone) in the central area, likely corresponding to the volcanic crater and low-density volcanic materials. In contrast, the surrounding gravity highs (red zones) may reflect denser basement rocks or volcanic edifice structures.

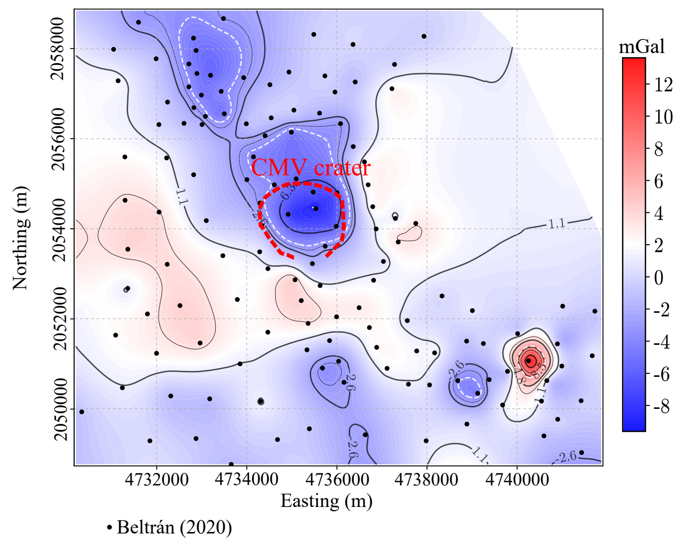

Figure 2: Residual gravity anomaly map in the CMGA. The contour map shows gravity anomalies ranging from -9.092 to 13.77 mGal, with blue areas representing negative anomalies (gravity lows) and red areas representing positive anomalies (gravity highs).

Notably, a prominent negative gravimetric anomaly, observed within the volcano's central and northern regions, was interpreted by Pedraza et al. (2022) and Herrera (2020) as representative of high-density intrusive bodies. Additionally, magnetotelluric surveys have identified resistivity contrasts interpreted as magmatic bodies and some prospective elements of the CMGA system. Recent three-dimensional resistivity models derived from magnetotelluric data have delineated a complex architecture including a potential magmatic reservoir at approximately 5 km depth and preferential fluid pathways along structural discontinuities (Herrera, 2020).

Despite these advances, integrated multi-method geophysical models remain limited in their scope. While magnetotelluric studies provide valuable insights into resistivity distribution, complementary property models, particularly density contrasts, are needed to comprehensively characterize the geothermal system's prospective elements (Miller et al., 2017). The availability of open-access geophysical datasets and accumulated geological knowledge of the volcanic system presents a significant opportunity for renewable energy research and development. Implementing advanced 3D gravity inversion models represents a crucial next step in characterizing this resource, potentially accelerating the clean energy transition by identifying viable geothermal reservoirs and optimal drilling targets for sustainable power generation in Colombia.

PROPOSED METHODOLOGY

The proposed methodology, outlined in Figure 3, was implemented using the open-source modeling and inver-

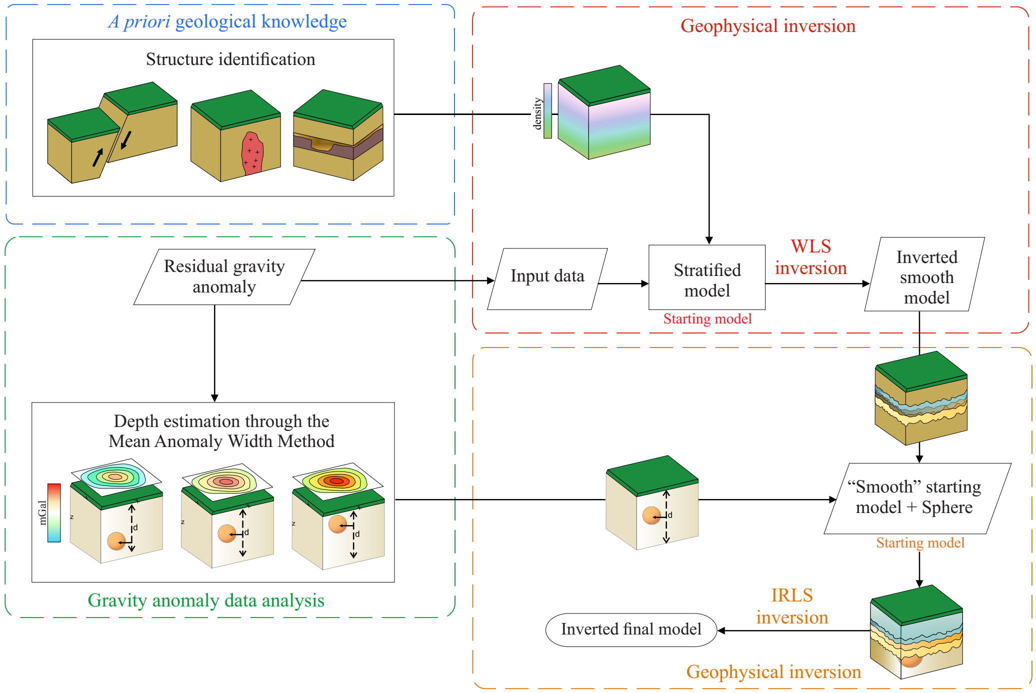

Figure 3: The workflow outlines the integration of anomaly data analysis in creating adaptive starting models for 3D gravity inversion using Weighted Least Squares (WLS) and Iterative Reweighted Least Squares (IRLS) regularization. It features two pathways: the upper pathway focuses on structural delineation through the analysis of *a priori* geological information to develop the starting model. In contrast, the lower pathway uses average width and depth estimation to characterize intrusive bodies for a second model. Both pathways converge in an integrated inversion framework that includes stratified models, WLS regularization, and soft constraints. The final inversion stage applies IRLS regularization to recover high-resolution subsurface density distributions, highlighting compact and deep geological features.

sion framework SimPEG (Cockett et al., 2015). We designed a two-stage inversion workflow with sequential regularization, incorporating *a priori* geological and geophysical information to construct two starting models in a comprehensive three-dimensional analysis. The first starting model was constructed from geological information that integrates conceptual models of the Cerro Machín Volcano with physical boundaries and is detailed in the appendix: Analysis of *a priori* geological information for the construction of an adaptive starting model for inversion with WLS regularization. The construction of the second initial model also incorporates physical boundaries and is detailed in depth in the appendix: Analysis of *a priori* geophysical information for IRLS inversion with adaptive initialization.

Mean Anomaly Width Method applied to the residual anomaly of the CMGA

For the two-phase sequential inversion approach, it was necessary to employ two starting models.

To construct the starting model, we adopted a structured and hierarchical approach to integrate the available geological and geophysical knowledge about the CMGA. The study that most clearly exemplified the features that our initial model needed was that presented by Pedraza et al. (2022). This body of knowledge was systematized by stratifying the subsurface into coherent units based on their interpreted lithological and physical properties, with particular attention to the identification of low-density volcanic deposits, intermediate-density sedimentary layers, and the deeper, high-density basement. Densities were not assigned arbitrarily, but were organized according to an internally consistent geological framework that took into account the vertical gradation trends commonly associated with burial depth and the properties of basement rocks.

No compact bodies were introduced at this stage; instead, the model had a smooth, vertically graded distribution, which preserved the model's function as a neutral reference configuration for the initial phase of the inversion. The resulting model provided a physically plausible and geologically sound representation of the subsurface, suitable for WLS regularization and designed to resolve smoothed features that are typically undetectable by direct anomaly analysis alone.

For this second stage, and to incorporate additional *a priori* constraints, an analysis of the residual gravitational anomaly was performed using the MAWM to construct the second starting model. In an early review of inverted models of the CMGA, Beltrán (2020) and Pedraza et al. (2022) identify a deep, compact, elongated body that they associate with a volcanic conduit.

Telford et al. (1990) indicates, through direct modeling techniques, that spheres best describe the gravimetric anomaly response of volcanic dikes or conduits, which is why we use a sphere for the MAWM. This method is described by equation (1), formulated by Dobrin and Savit (1960), in which the parameter $X_{1/2}$ represents half the width of the gravimetric anomaly, defined as the horizontal distance between the maximum of the anomaly and the points on either side where its amplitude decreases to half the maximum value

$$Z \approx 1.305 \cdot X_{1/2} . \quad (1)$$

This geometric parameter was extracted directly from the anomaly profile and used to estimate the depth to the center of a buried sphere using an empirical relationship. The depth of the center of the sphere is obtained by solving for Z in the equation (1), once half the width of the gravimetric anomaly is known. The estimate of the sphere's radius is obtained from equation (2), which describes the response of the maximum anomaly on a sphere solved for R (radius), where G is the gravitational constant, Δg_{max} is the maximum amplitude of the anomaly, and $\Delta\rho$ is the density contrast value for the sphere

$$R = \left(\frac{3\Delta g_{\max} Z^2}{4\pi G \Delta\rho}\right)^{1/3} . \quad (2)$$

The second starting model, used in the second stage of inversion, is constructed by taking as a reference the density contrast model with smoothed and shallow layers recovered from the WLS inversion and adding the sphere determined through the MAWM analysis. In this stage of the inversion, IRLS regularization was applied, promoting spatial dispersion and adaptively improving the compactness of the model, thus obtaining more compact bodies (Zhu et al., 2024).

We used WLS-type regularization in the first stage and then IRLS, based on the fact that incorporating smoothed and shallow information into an inversion yields better solutions for obtaining compact models through iterative weight updating, which preserve the *a priori* information of smoothed and shallow layers (Constable et al., 1987). This sequential and adaptive inversion framework enhances the resolution of both shallow and deep density anomalies, yielding a final model suitable for geological interpretation.

3D inversion with sequential regularization

We solve the inverse problem through using the WLS and IRLS regularization approaches subsequently defined by Tikhonov and Arsenin (1977), as a composite objective function:

$$\Phi(\mathbf{m}) = \Phi_d(\mathbf{m}) + \beta\Phi_m(\mathbf{m}) . \quad (3)$$

The Tikhonov parameter, represented by β in equation (3), is a positive scalar that regulates the balance between data fit and model structure in the predicted function. A small β yields a model that fits the data well, but it may also have an excessive structure, which would lead to a large model norm, $\Phi_m(\mathbf{m})$. Optimization results in a larger data adjustment $\Phi_d(\mathbf{m})$, and a model with a minimum structure if β is significant. This method continues until the algorithm converges to a minimum and reaches the tolerance of misfit (Tikhonov and Arsenin, 1977).

ℓ_2-norm regularized objective function

The objective function defined in equation (4), considered as misfit function $\Phi_d(\mathbf{m})$ the typical ℓ_2-norm that weights the mismatch between $\mathbf{d}^{obs}$ which represents the observed data, and $\mathbf{G}(\mathbf{m})$ is the mathematical expression of the forward modeling problem that determines the geophysical observations given a particular model $\mathbf{m}$, through the uncertainty matrix $\mathbf{W}_d = \mathrm{diag}\{1/\sigma_1, 1/\sigma_2, \cdots, 1/\sigma_n\}$, where σ is the estimated standard deviation of observation error in the n_{th} data. The model norm $\Phi_m(\mathbf{m})$ contains the weighting matrices, depth weighting matrix or distance weighted $\mathbf{W}_i$, which measure the amount of model structure and the spatial roughness of the recovered model and the indices $i = s, x, y, z$ denote, respectively, the smallest model component and the smoothness components in the x-, y-, and z- directions (Li and Oldenburg, 1996; Oldenburg and Li, 2005; Aster et al., 2018). Constant $\alpha_i (i = s, x, y, z)$ represents the weighting parameter on each component in

$$\Phi(\mathbf{m}) = \left\| \mathbf{W}_d \left(\mathbf{d}^{obs} - \mathbf{G}(\mathbf{m}) \right) \right\|_2^2 + \beta \sum_{i=s,x,y,z} \alpha_i \left\| \mathbf{W}(\mathbf{m}) \right\|_2^2 . \quad (4)$$

In equation (5), we adopt standard deviations per data point σ_i to reflect the minimum reduction limits and the modeling error proportional to the amplitude. We assume heteroscedastic errors composed of an additive "minimum" plus a component proportional to the signal amplitude. For data i, in

$$\sigma_i = \sqrt{\sigma_{\text{floor}}^2 + (\sigma_{\text{rel}} |\mathbf{d}_i^{obs}|)^2} , \quad (5)$$

the term $\mathbf{d}_i^{obs}$ is the gravitational anomaly observed in data i, σ_{floor} is a lower limit of uncertainty that captures the repeatability of the instrument and levels out positioning errors, and σ_{rel} is a dimensionless coefficient that models the uncertainty and scale with the magnitude of the anomaly. Errors in gravity data are rarely uniform. This choice combines a fixed "floor" term accounting for instrument and leveling errors with a relative term that scales with the anomaly amplitude, thereby stabilizing the inversion across regions of varying signal strength (Li and Oldenburg, 1998; Farquharson and Oldenburg, 2002; Pedersen and Rasmussen, 1990).

Rather than encoding *a priori* geology in a reference model, we embed it in the starting model and set reference model=0; this guides the search without biasing the regularization toward a prescribed reference (Cockett et al., 2015). Minimizing equation (4), which we used for our first WLS inversion, leads to a smooth solution, which is unexpected for characterizing geological structures with well-defined boundaries.

Because potential field data lacks intrinsic depth resolution, depth weighting is used in gravity inversion to offset the decay of the kernels with depth. Through equation (6), we implemented an updated approach of depth weighting function, initially proposed by Li and Oldenburg (1996, 1998), as follows,

$$W(z) = (|z - z_0| + \epsilon)^{-\nu/2} , \tag{6}$$

where z_0 is a small positive constant introduced to avoid singularities near the surface, z is the vector of cell depths in the discretized mesh, ϵ is a threshold value, and ν is the depth weighting exponent, typically ranging between 0.5 and 3, with a conventional value of 2 for gravity inversion (Oldenburg and Li, 2005). This range provides a physically reasonable range that stabilizes the inversion while counteracting the kernel decay, where smaller values ($\nu \approx 0.5$) apply mild compensation suitable for shallow sources, whereas larger values ($\nu \approx 2-3$) enhance the contribution of deeper cells (Li and Oldenburg, 1996). The proposed methodology combines depth weighting with conventional model weighting, enabling the incorporation of targeted regularization strategies informed by *a priori* geological knowledge (Lelièvre and Oldenburg, 2009; Miller et al., 2020), to be incorporated with a weighting matrix $\mathbf{W}_i$ presented in the equation (7)

$$\mathbf{W}_i = \mathrm{diag}\left(W(z)\right) . \tag{7}$$

If we use general measures of the length of vectors, the above objective function would become

$$\Phi(\mathbf{m}) = \Phi_d^g \left[\mathbf{W}_d(\mathbf{d}^{\mathrm{obs}} - \mathbf{G}(\mathbf{m}))\right] + \beta \sum_{i=x,y,z} \alpha_i \Phi_i^g \left[\mathbf{W}_i(\mathbf{m})\right] \tag{8}$$

where Φ_d^g is a symbolic representation of the data misfit function defined by a general measure, similar notation is used for the second term.

Iterative process of updating the starting model

The use of general measures causes the objective function to be non-quadratic, and the minimization must be solved iteratively regardless of whether the forward problem is linear or not. To solve the non-linear minimization in equation (8), it is optimal to use the Projected Gauss–Newton Conjugate Gradient, which is a hybrid method that combines the efficiency of the Conjugate Gradient with the linear approximation of Gauss–Newton, and the word Projected refers to the fact that it imposes physical limits on each iteration to avoid unrealistic density values. Assume we obtain the solution denoted by $\mathbf{m}^{(k+1)}$ at the $(k+1)$th iteration, and the predicted data corresponding to this model are $\mathbf{d}^{(k+1)}$. Then at the kth iteration, we minimize the following objective function to produce a model perturbation $\Delta\mathbf{m}$ so that the inverted model can be updated by $\mathbf{m}^{(k)} = \mathbf{m}^{(k+1)} + \Delta\mathbf{m}$:

$$\begin{aligned}\Phi(\mathbf{m}) = \Phi_d^g &\left\|\mathbf{W}_d\left(\mathbf{d}^{\mathrm{obs}} - \mathbf{G}(\mathbf{m}^{(k+1)} + \Delta\mathbf{m})\right)\right\| \\ &+ \beta \sum_{i=s,x,y,z} \alpha_i \Phi_i^g \left\|\mathbf{W}_i(\mathbf{m}^{(k+1)} + \Delta\mathbf{m})\right\| .\end{aligned} \tag{9}$$

Appendix A shows how equation (8) produces the following equation, which must be solved for the perturbation model $\Delta\mathbf{m}$:

$$\begin{aligned}&\left[\mathbf{J}^{\mathsf{T}}\mathbf{W}_d^{\mathsf{T}}\mathbf{R}_d\mathbf{W}_d\mathbf{J} + \beta \sum_{i=s,x,y,z} \alpha_i\, \mathbf{W}_i^{\mathsf{T}}\mathbf{R}_i\mathbf{W}_i\right]\Delta\mathbf{m} \\ &= \mathbf{J}^{\mathsf{T}}\mathbf{W}_d^{\mathsf{T}}\mathbf{R}_d\mathbf{W}_d\left(\mathbf{d}^{\mathrm{obs}} - \mathbf{d}^{(k+1)}\right) \\ &\quad - \beta \sum_{i=s,x,y,z} \alpha_i\, \mathbf{W}_i^{\mathsf{T}}\mathbf{R}_i\mathbf{W}_i\left(\mathbf{m}^{(k+1)}\right) ,\end{aligned} \tag{10}$$

where $\mathbf{J}$ is the sensitivity matrix, and $\mathbf{R}_i$ are diagonal matrices whose diagonal elements are determined by the choice of general measures. Solution of equation (10), yields the model perturbation $\Delta\mathbf{m}$ for updating the model $\mathbf{m}^{k+1}$. The inversion then proceeds to the next iteration.

We solve equation (9) by a matrix-free Conjugate Gradient (CG) inner iteration and update the model through a projected line-search step, getting the equation (11),

$$\mathbf{m}^{(k+1)} = \mathrm{Proj}_{[\mathbf{m}_{\min},\mathbf{m}_{\max}]}\left(\mathbf{m}^{(k)} + \gamma^{(k)}\Delta\mathbf{m}\right) , \tag{11}$$

with γ^k chosen by backtracking to satisfy sufficient decrease, and with bound constraints enforced by projection (Cockett et al., 2015).

$\Delta\mathbf{m}$ is subject to the impact of the parameters' smallness and smoothness, so the influence of $\mathbf{R}_d$, $\mathbf{R}_s$, $\mathbf{R}_x$, $\mathbf{R}_y$, $\mathbf{R}_z$ is implicit. To understand in depth how the $/ell_p$ standard is implicit, it is necessary to refer to Appendix B

RESULTS AND DISCUSSION

The 137 residual gravity anomaly data used in our inversion were taken from Beltrán (2020) across the entire CMGA domain and were not modified or reworked. The starting models described below in the following two appendices were used in the inversion process and were discretized on a regular tensor mesh with a base cell size of 250 m, extending 11 km in the north-south direction, 12 km in the east-west direction, and 10 km in the vertical direction. The mesh cell size corresponds to the distance between the gravimetric stations in the study, with the distance between stations greater than 265 m and the cell size smaller than this distance. This allows regional structures to be appreciated with good resolution through a mesh that is not computationally very expensive.

Analysis of *a priori* geological information for the construction of an adaptive starting model for inversion with WLS regularization

To define the absolute density values for the model, we used the regional reduction density of 2629 kg/m^3 determined by Beltrán (2020) as a baseline. This value served as the reference around which contrasts were calculated. Pedraza et al. (2022) further constrained the density range by reporting average values of approximately 2300 kg/m^3 for unconsolidated volcanic deposits and up to 2900 kg/m^3 for basement lithologies attributed to the Cajamarca metamorphic complex. These constraints were used to define a vertical density gradient within the model, ranging from a minimum contrast of −300 kg/m^3 near the surface to a maximum of +300 kg/m^3 at depth, relative to the reference density.

The model was constructed as a smooth gradient without abrupt transitions, reflecting the gradual lithological changes expected in sedimentary and volcanic sequences. This configuration enabled the model to serve as an effective prior for the WLS inversion, with a focus on recovering large-scale, diffuse density anomalies. By avoiding the imposition of artificially compact structures at this stage, the model ensured that subsequent inversions would not be biased toward unrealistic geometries, but instead would be guided by the regional geological framework and depth-dependent density trends derived from validated sources.

Implementation details for WLS inversion: we use the σ value as the standard deviation for each value, with a relative error of 0.02, floor uncertainty of 0.050 mGal, $\alpha_s = 10^{-4}$, $\beta = 1.0$, and a starting model whose density increases with depth, which converged in a recovered model after 20 iterations.

The assignment of uncertainty to gravity observations reflects instrumental accuracy and environmental noise characteristics typical of volcanic terrain. The same uncertainty is implicitly present in the residual anomaly data, since it originates from observed measurements and therefore carries the propagated instrumental and environmental noise. The value we assign to the Tikhonov parameter β prioritizes data fitting and model smoothness, and assigns moderate importance to the starting model (Cockett et al., 2015).

The WLS inversion integrated the starting smooth model shown in Figure 4a, which shows a progressive increase in density as depth increases, which is why its maximum density contrast value (300 kg/m^3) is at depth. Its lowest value is at shallow depth (-300 kg/m^3). The integration of this model allows for the recovery of smoothed structures in shallow areas and their differentiation from the basement, which, as demonstrated in previous studies, has a higher density. The small parameter α_s, which controls the relative weight of the starting model on the inverted model, takes on a small value, causing our starting model to have a moderate influence on the final inversion process, giving more importance to the data fit. Likewise, the density contrast range was altered, allowing the lower limit to reach -400 kg/m^3, which enabled us to uncover low-density bodies embedded in the subsurface and associated with highly negative anomalies.

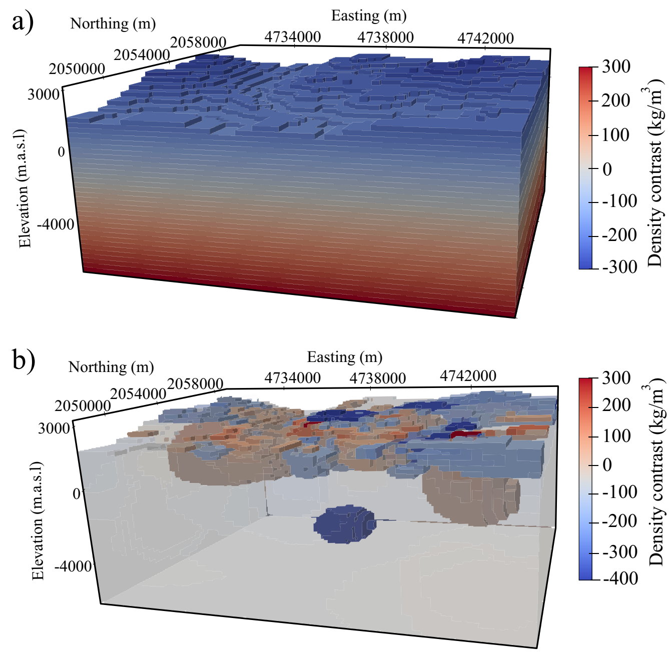

Figure 4: Starting models created from the interpretation of the residual anomaly data from the CMGA with density contrast inferred through the Pedraza et al. (2022) model and the base density shown by Beltrán (2020). a) Starting model corresponding to the WLS inversion whose density increases with increasing depth and has a density contrast of -300 kg/m^3 to 300 kg/m^3. b) Inverted model with WLS regularization that is used as an starting model for the IRLS inversion with density contrast of -400 kg/m^3 to 300 kg/m^3.

This inversion was designed to recover large-scale, smoothed shallow structures by applying WLS regularization. The use of the ℓ_2-norm in the regularization term quadratically penalizes deviations, thereby enforcing smoothness and continuity relative to the starting model. As a consequence, the inversion tends to preserve gradual transitions in physical properties, enhancing the recovery of diffuse features while simultaneously attenuating or displacing compact anomalies often rendering them artificially shallow or laterally expanded.

Analysis of *a priori* geophysical information for IRLS inversion with adaptive initialization

The starting model obtained through WLS inversion, constrained by the ℓ_2 regularization that penalizes large structures and stratigraphic gradients, successfully resolved broad low-density structures at shallow depths (2700 to 0 m.a.s.l.). However, due to the inherent smoothing effects of the regularization, it lacked the resolution required to delineate high-gradient, compact features at depth. To overcome

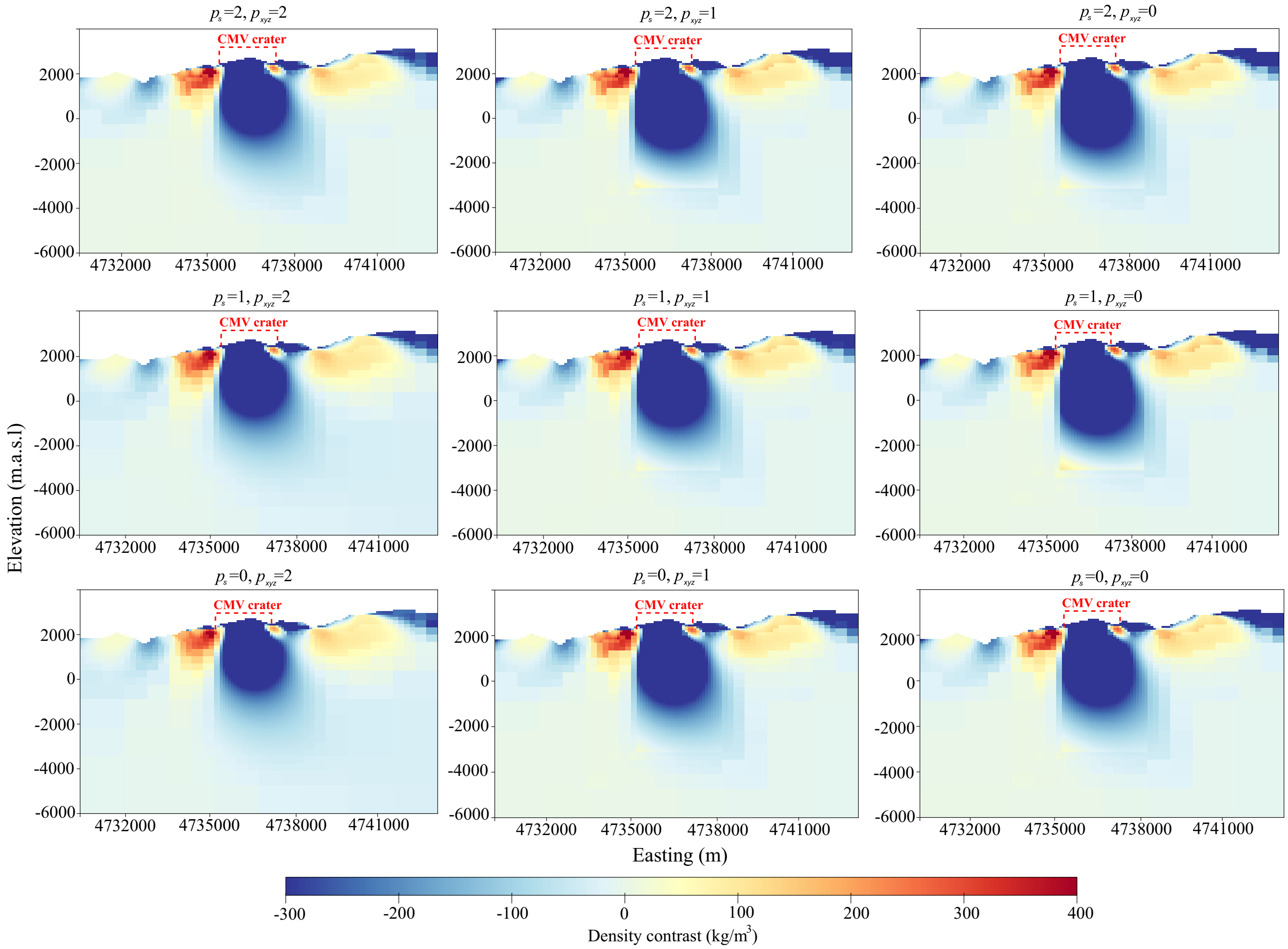

Figure 5: 3D gravity inversion using IRLS with different p norms (from $p = 2$ to $p = 0$). The blue structure represents a high-density volcanic conduit. Lower norms (especially $p = 0$) yield sparser and better-defined solutions of the conduit.

this limitation and construct a more geologically informed second starting model, we isolated the residual anomaly associated with the most prominent negative gravimetric signal of -9.092 mGal located in the central region of the CMV dome. We applied a model-independent MAWM analysis (Blaikie et al., 2014). This technique was used to estimate the depth and lateral extent of the sphere.

To determine the geometry of the buried mass, we apply the MAWM to the localized anomaly profile. Given that the horizontal distance is X = 3.4 km (equivalent to the width of the signal), and the maximum value of the anomaly is -10 mGal, the average width of the signal is calculated as $X_{1/2} = 1.7$ km. This width, together with the amplitude of the anomaly and a minimum density contrast of $\Delta\rho = -300$ kg/m^3, due to the minimum value of the anomaly indicating a mass deficit, was used to calculate the radius and depth of an equivalent buried sphere, reorganizing the analytical solution of the gravitational effect of a spherical body.

The estimated sphere, representing a compact low density anomaly, was incorporated into the original WLS model to produce the second starting model. It was centered at coordinates E: 4735320 m, N: 2054777 m, and following the equation (1) we obtain Z: −2200 m.a.s.l, with a radius R ≈ 1790 m, which we estimate with the equation (2). This updated starting model thus integrates both the large-scale, vertically graded background density structure and the localized, high-contrast feature inferred from the residual anomaly analysis. By doing so, it provides a more effective initialization for the subsequent IRLS inversion, enabling better recovery of compact bodies at depth while maintaining the smoothed representation of shallower layers.

Implementation details for IRLS inversion: we use the σ value as the standard deviation for each value, with a relative error of 0.02, floor uncertainty of 0.050 mGal, $\alpha_s = 10^{-4}$, $\beta = 1e-4$, $z_0 = 3$, with a depth weighting exponent $\nu = 2$ and A step length γ calculated using the solver with a maximum number of trials = 60 and a factor of 0.2. We also use an ℓ_p-norm with a value of $[2, 1, 1, 1]$ and a starting model of smooth and shallow bodies with a high-contrast sphere of density, which converged to a

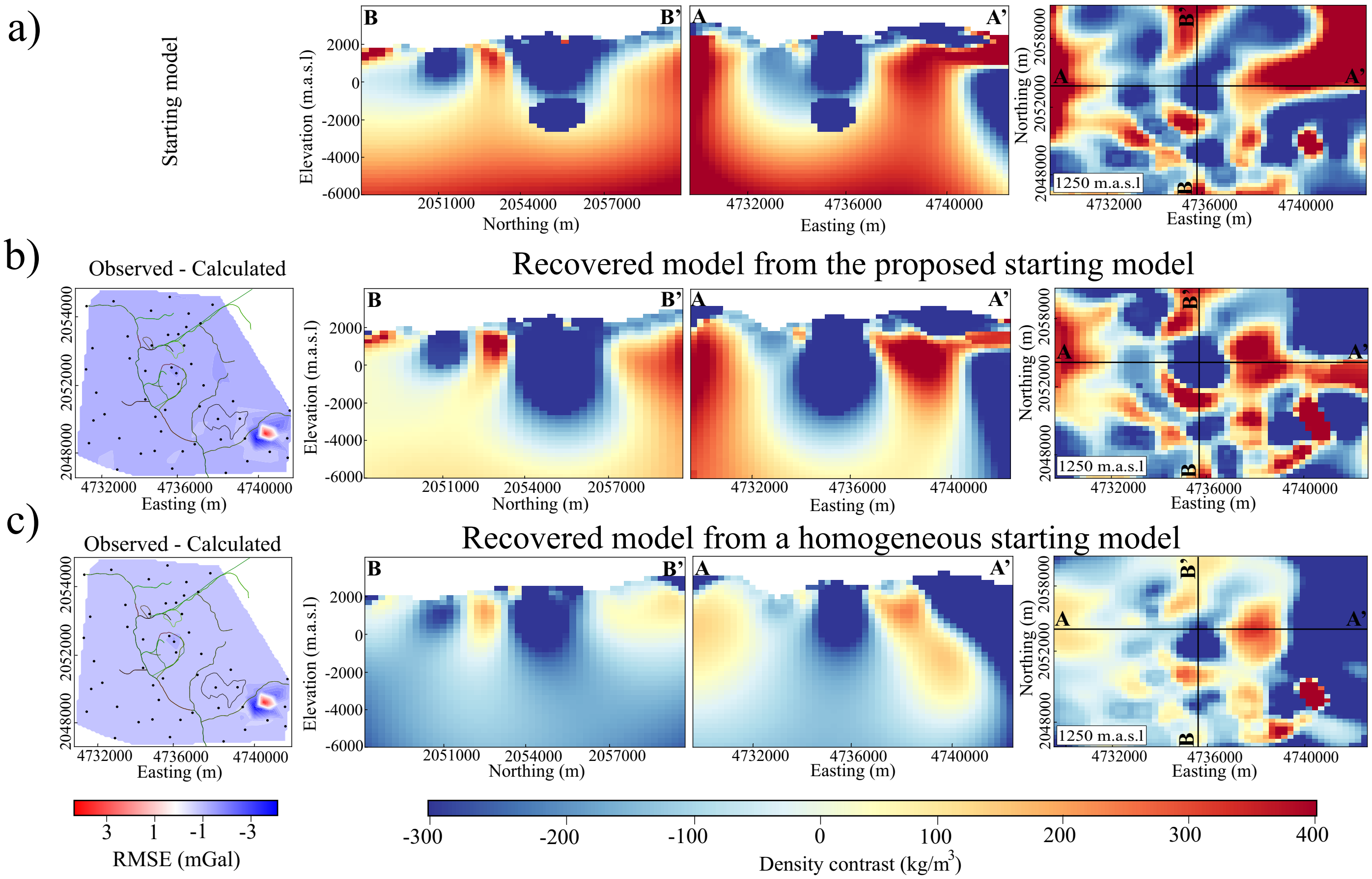

Figure 6: Comparison between the models recovered from the IRLS inversion, showing a) the proposed starting model, b) the inverted model with the proposed starting model from figure a), and c) an inverted model based on a homogeneous starting model. The compared models have a cut in z, north, and east, presenting the RMSE of both compared models.

model after 20 iterations.

For subsequent investment with IRLS regularization, the parameters σ_s and Tikhonov β were kept low and gradually decreased in the iterative process to give weight to the starting model and favor the creation of compact structures in depth. The configuration of the depth- weighting function was crucial in counteracting kernel decay and avoiding surface singularities. According to Li and Oldenburg (1998), a value of $z_0 \geq 2$ compensates for the excess weighting near the surface without forcing the mass to too deep a depth. Through a moderate step length, we keep our model close to the geological solutions provided by the starting model, thereby accelerating the model's convergence as is shown in the Figure 8a. The sphere located in depth contributed to the recovery of deep and compact structures by guiding the inversion along the shortest route toward the convergence of bodies.

Figure 5 shows the analysis of the ℓ_p-norm to evaluate the suitability of the different regularization parameterizations in our final model. In this experiment, the mesh was refined to a cell size of 100 m to determine which values of $\mathbf{P}$ yielded the best RMSE result and best recovered the body in depth. This strategic approach capitalizes on the inherent non-uniqueness of potential field inversion, allowing for the incorporation of geological expectations and enabling the adaptive refinement of subsurface structures through the optimal selection of regularization norms. The minimum and maximum density-contrast values displayed in Figure 6 correspond to the physical bounds imposed in the inversion ($\mathbf{m}_{min}$ and $\mathbf{m}_{max}$) rather than the absolute extremes of the recovered model. These bounds were defined according to petrophysical constraints and geological information of the CMGA lithologies (volcanic, pyroclastic, and metamorphic units), which typically range between -300 and +400 kg/m^3 relative to the regional reference density. The use of these bounds prevents nonphysical oscillations and ensures that the recovered densities remain consistent with plausible rock properties, as recommended by Li and Oldenburg (1998); Oldenburg and Li (2005); Sun and Li (2014).

A systematic exploration of the regularization parameter space was conducted by varying the ℓ_p-norm values applied independently to different components of the model objective function. Specifically, nine combinations were tested for the norm tuple $\mathbf{p} = [p_s, p_x, p_y, p_z]$, where p_s controls the sparsity of the model amplitude, and p_x, p_y, and p_z are applied to the spatial derivatives along the x, y, and z directions, respectively. The tested combinations included: $[0,0,0,0]$, $[0,1,1,1]$, $[0,2,2,2]$, $[1,0,0,0]$, $[1,1,1,1]$, $[1,2,2,2]$, $[2,0,0,0]$, $[2,1,1,1]$, and $[2,2,2,2]$.

The choice of norm configuration had a significant influence on the morphology of the recovered density structures. Sparse model norms ($p_s = 0$) promoted isolated, compact bodies, while smoother spatial derivative norms ($p_x = p_y = p_z = 2$) enhanced lateral continuity. Intermediate configurations led to varying degrees of compactness and smoothness: for instance, $\mathbf{p} = [1,1,1,1]$ produced blocky structures, whereas $\mathbf{p} = [2,0,0,0]$ yielded vertically elongated features. Convergence metrics, such as changes in the objective function and RMSE stabilization, were monitored during each inversion and are summarized in Table 1. The lowest RMSE was obtained using the norm configuration $\mathbf{p} = [2,1,1,1]$, therefore, it was chosen as the best combination of ℓ_p standard for our inversion.

Table 1: Norm combinations $\mathbf{p} = [p_s, p_x, p_y, p_z]$ used for regularization terms and their corresponding RMSE values. The lowest RMSE was obtained for the combination $\mathbf{p} = [2,1,1,1]$ under IRLS inversion.

$\mathbf{p}$	RMSE (mGal)
$[0,0,0,0]$	0.4730
$[0,1,1,1]$	0.1707
$[0,2,2,2]$	0.1665
$[1,0,0,0]$	0.2366
$[1,1,1,1]$	0.1901
$[1,2,2,2]$	0.2480
$[2,0,0,0]$	0.2447
$[2,1,1,1]$	**0.1375**
$[2,2,2,2]$	0.2461

The Figure 5 shows that optimal results were obtained with the ℓ_p norm setting $[2,1,1,1]$, which successfully balanced the conflicting requirements of compact amplitude distribution and smooth spatial transitions. This scheme facilitated the generation of bodies and layers smoothed at shallow, as well as a well-defined vertical conduit extending from a depth of -3000 m above sea level to a few meters below the surface, showing density contrasts of -300 to 0.0 kg/m^3 relative to the host rocks. The recovered structure has a funnel-shaped geometry, with a narrow throat (about 500 m in diameter) at depth that expands to about 1000 m in diameter near the surface, consistent with the morphologies of volcanic conduits observed through geophysical imaging in analogous systems. Smooth gradient constraints (p_x, p_y, $p_z = 1$) prevented artificial segmentation, while the scattered amplitude norm ($p_s = 2$) concentrated low-density material along the central axis.

Defining the role of starting models in IRLS inversion

The Figure 6 shows the contrast between both inverted models and allows us to see that although both inversions use an IRLS regularization with ℓ_p norms that favor compactness, it is very difficult for the inverted model from an starting homogeneous model to converge compact and non-diffuse structures at depth that make geological sense.

Low β values place almost all the weight on the data fit. This amplifies the problem of non-uniqueness of solutions in our final inverted model, as we would disadvantage geological solutions in order to prioritize an unreasonable density model that fits the data. However, the low value of α_s, which allows for high density contrasts, accompanied by a short step size and an starting model that "guides" and brings our solutions closer to geological approximations, allows us to obtain a model with compact bodies, well-defined edges, and geological consistency as is shown in 6.

Unlike a common homogeneous starting model, which lacks representative structures and does not contribute to the understanding of the observed data, our proposed starting model incorporates the expected density distribution, represented as *a priori* information, which facilitates convergence and prevents the algorithm from getting stuck in local minima.

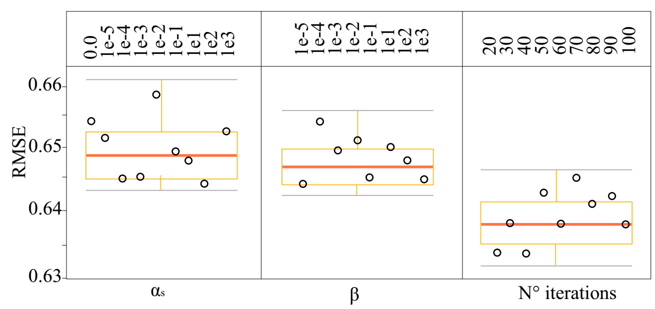

Figure 7: The box plot of the RMSE obtained if any of these parameters (α_s, β, number of iterations) takes the value found at the top, while the other parameters remain static.

In this context, the parameter β controls the relative weight of the starting model in the objective function: higher values of β increase the influence of the starting model on the final solution. In comparison, lower values favor a freer fit to the data. In turn, the α_s parameter modulates the effective integration of the starting model into the estimated model; an appropriate α_s allows the inversion to preserve the essential structures of the starting model, while adjusting them consistently with the observed gravimetric response. In this study, the smallness weight α_s was intentionally set to a low value in order to relax the constraint between the recovered and starting models. According to Li and Oldenburg (1996, 1998), a small α_s allows the inversion to depart from the starting model where required by the data, while still preserving its overall structure through the spatial derivative terms $(\alpha_x, \alpha_y, \alpha_z)$. This configuration is particularly suitable for the sequential WLS–S-IRLS scheme, where the geologically informed starting model serves only as a guide rather than a fixed reference. The low α_s therefore ensures that new compact structures can emerge in depth without imposing an excessive bias from the starting model.

Additionally, the iterative update of the model parameters is scaled by the step length γ, which determines the size of each correction during optimization. In this study, a low value of $\gamma = 0.2$ was adopted after testing multiple configurations. The choice of a low γ factor, in addition to maintaining a short step, provided a balance between stability and convergence speed: smaller values of γ resulted in overly conservative updates that delayed 665 convergence In contrast, huge values produced oscillatory behavior and risked divergence, increasing model convergence times.

It is noteworthy that the inversion was guided by an starting model constructed from *a priori* geological information, rather than by imposing a fixed reference model. This strategy provides greater flexibility in contexts characterized by high geological uncertainty, as the inversion is not constrained to remain close to an arbitrary reference but is instead free to explore a broader solution space. At the same time, because the starting model was designed to be geologically plausible and already aligned with the expected density distribution, the optimization process required fewer iterations to converge toward a stable solution. In practice, this reduced the risk of the algorithm becoming trapped in non-physical local minima while also improving computational efficiency and accelerating the recovery of geologically consistent density contrasts. In the same way and to show the stability of the inversion made, in the Figure 7 shows how the parameters of β α_s and the number of iterations are varied to verify that the true advantage of this methodological approach does not lie in the inversion parameters but in the introduction of an starting model capable of guiding the inversion in a minimum number of iterations. Therefore, we shows that, by presenting an inversion methodology that is inherently close to the expected result, the proposed method also manages to reach the best data mismatch with the same number of iterations but in less time.

The result is a more accurate reconstruction of the geometries and density contrasts, preserving geological consistency throughout the inversion domain.

With the parameters $\mathbf{W}_d$, $\mathbf{W}_i$, α_i, mesh, and β-cooling fixed, the two curves isolate the effect of initialization on a nonconvex IRLS problem. Both trajectories follow the expected Tikhonov exchange Φ_d decreases while Φ_m increases—as β cools (β labels). At the target misfit Φ_d^*=135 mGal, the proposed start reaches a lower Φ_m than the homogeneous start, which means a simpler model for the same fit. It also reaches acceptance faster (1m56s vs 2m32s), implying cheaper inner solves along its GN–IRLS path. Together, these observations justify the claim that the proposed WLS-initialized IRLS pipeline achieves a better trade-off point and greater computational efficiency than IRLS started from a homogeneous model. The first inversion has a shorter time, indicating fewer or cheaper internal CG iterations (better conditioning) along the GN-IRLS path. Quote the times directly from the graph.

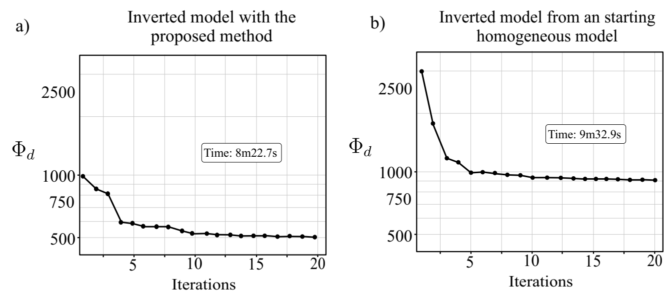

Figure 8: Tikhonov trade-off trajectories for two inversion pipelines. (a) Proposed WLS-IRLS initialization: iteration-wise evolution of data misfit versus model penalty under a common β-cooling schedule and the time required for the conversion of this model. (b) Homogeneous-start IRLS with the same parameters and the respective time of conversion. Filled symbols mark the accepted solutions at the target misfit (horizontal line).

Understanding the conceptual model of the Cerro Machín Geothermal Area

Herrera (2020) correlates conductive layers with zones of hydrothermal alteration, which are the result of the interaction of geothermal fluid with the host rock, which acts as a seal for the reservoir. Likewise, it indicates that if a seal layer exists in the geothermal system, it would be represented by small, shallow conductive structures located at depths of less than $\approx$ 700 m.

The three-dimensional representation of the conceptual model in Figure 10 of the CMGA geothermal system provides a comprehensive view of the subsurface architecture, outlining the intricate interconnection of its fundamental components. The primary pathways for heat and fluid advection from this source are the volcanic conduit. It is particularly relevant that the main volcanic conduit exhibits a predominant northwest (NW) trend in the model, which leads us to infer that the heat source or main magma chamber could be preferentially located or extend in that direction.

The structure of the inverted conduit shows a remarkable spatial correlation with conductive features identified by Herrera (2020) in magnetotelluric models, where resistivity values $\approx$1.3 $\Omega{\cdot}$m delineate a sub-vertical zone coincident with our recovered density anomaly. This correspondence supports the interpretation of an active volcanic-geothermal conduit that facilitates the transport of heat and fluids from deep magmatic sources. This body has its upper limit at 1000 m.a.s.l. and its lower limit at -4000 m.a.s.l., respectively, and narrows as it ascends, forming a kind of funnel, as shown in Figure 9.

The areas with negative lows and mass deficit that express responses in mGal between -2.0 and 0.0 indicate alteration zones, hydrothermal deposits, and volcanoclastic flows with high porosity interpreted as recharge zones (Wei et al., 2025). This interpretation aligns with established conceptual models of the CMGA, where extensive pyroclastic flow deposits and hydrothermally altered vol-

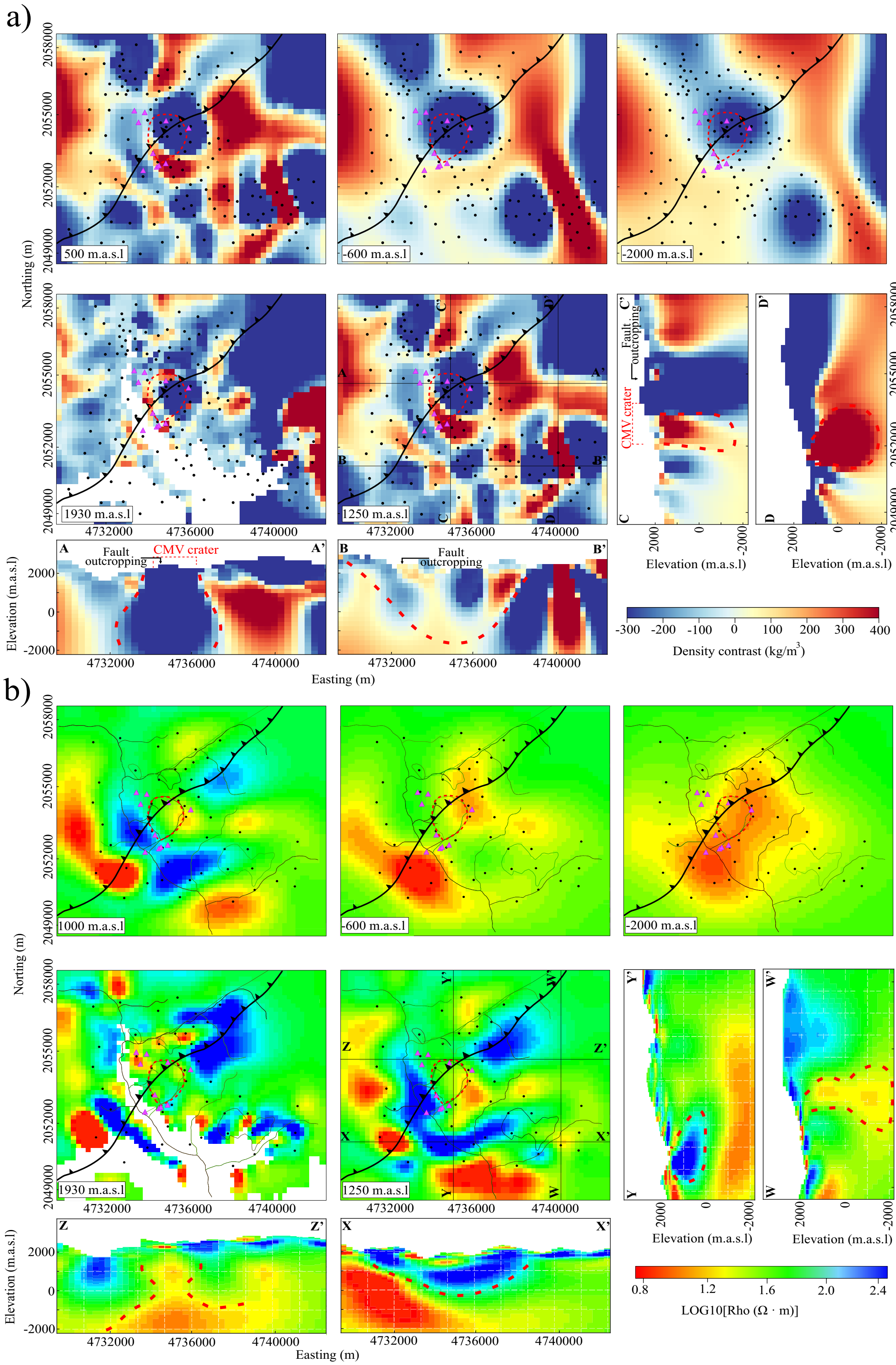

Figure 9: Cross-sectional views of inverted density models through various cross-sections and longitudinal sections. Density contrast values range from -300 to +400 kg/m^3, where blue indicates low-density areas and red represents high-density regions. Below are inverted magnetotelluric profiles made by Herrera (2020), where high resistivity values are represented in blue and low resistivity values in red. The fault traced on the surface is proposed by Mosquera et al. (1982), the dotted red line indicates the horseshoe-shaped CMV crater on the surface, while the purple triangles denote areas of hot springs and the black spots are the measuring stations.

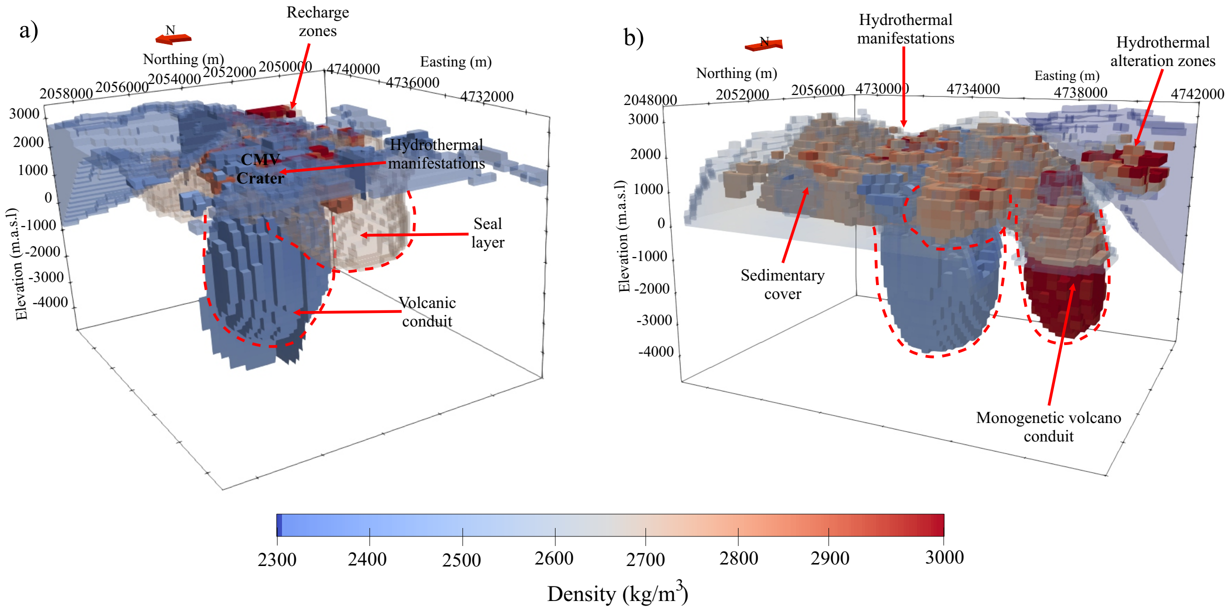

Figure 10: Three-dimensional conceptual geological-geophysical model of the CMGA system, depicting density distribution. a) View highlighting key geothermal components, including the CMV Crater, shallow hydrothermal manifestations, and a confining seal layer. b) Alternative view illustrating the shallow hydrothermal features, sedimentary cover acting as a cap rock, and the inferred monogenetic volcano conduit (blue body, representing a low-density anomaly). The model integrates structural and density information to conceptualize the surface expressions of the geothermal system.

canic sequences create significant density contrasts relative to the crystalline basement.

Pedraza et al. (2022) suggests, through its conceptual density model, the presence of structures similar to volcanic conduits with lower absolute density values in contrast to the basement. Furthermore, the magnitude of the absolute density (2300 to 2500 kg/m^3) is within the expected ranges for steam-dominated conduits and brecciated volcanic necks, as documented in comparative studies of siliceous volcanic systems (Miller et al., 2017; Trevino et al., 2021). Similarly, the peripheral zones maintained intermediate density values (2700 kg/m^3), representing the allegedly hydrothermally altered wall rock, because these densities align with those presented by Witter et al. 2016.

Additionally, the bright red body in the model, associated with the “Monogenetic volcano conduit,” is interpreted as a presumed conduit of a monogenetic volcano, representing another significant pathway for fluid migration. Permeability in the deep system is enhanced not only by these magmatic conduits but also by a complex network of regional structures.

In the shallow portions of the system, the model illustrates a “Seal layer” and a “Sedimentary cover,” which act as cap rocks. These units are characterized by relatively higher densities of 2850 kg/m^3 (reddish tones in the model), similar to those of aims Wei et al. (2025), which is in a very similar geothermal context, compared to the anomalies of the conduits, which is consistent with their low intrinsic permeability. Their role is fundamental in confining geothermal fluids within the reservoir, maintaining optimal pressure and temperature for resource exploitation, and preventing uncontrolled heat dissipation. The geothermal reservoir, although not explicitly labeled, is inferred from the rock volumes adjacent to the conduits and the heat source, where permeability develops through secondary porosity in the high-density basement and the overlying volcanic deposits. The hydrothermal alteration zones represented in the shallow portion of the model exhibit predominantly low densities of 2300 kg/m^3 (blue tones), which is consistent with hydrothermal alteration processes that can generate lower-density minerals or increase porosity due to leaching. According to Gutiérrez (2020), the presence of minerals such as epidote in these zones is a strong indicator of rock-fluid interaction at high temperatures and high densities.

The successful recovery of this feature demonstrates the effectiveness of combining smooth starting models from WLS inversion with focused IRLS refinement, providing a two-phases methodology for imaging complex volcanic plumbing systems where both distributed and concentrated density anomalies coexist.

CONCLUSIONS

This research highlights the crucial role of incorporating geological *a priori* information through carefully designed starting models in gravity inversion algorithms for volcanic-geothermal systems. The sequential inversion methodology, which combines WLS with an initialization with geological constraints followed by IRLS refinement, successfully resolved the convergence of compact bodies at depth, with optimal times and the obtaining of geologically reasonable models for the CMGA area. The key innovation lies in the systematic integration of geological knowledge into the inversion workflow for the construction of starting models capable of improving IRLS inversion by promoting well-defined and less smoothed edges at depth. The starting model, accompanied by a regularization that guided it toward the recovery of compact and deep structures, recovered focused volcanic conduits without converging on non-geological solutions, an indicator that we are approaching the global minimum we are seeking. The optimal setting of the norm $[2, 1, 1, 1]$ effectively captured the volumetric distribution of the CMGA bodies in a manner that satisfied the data. The stability of the designed scheme was demonstrated through statistical analysis, which established the methodology as an alternative to traditional inversion that takes advantage of *a priori* information and robust starting models. This methodological framework also demonstrated the capabilities of starting models for use in highly complex inversions by streamlining and making the process more efficient, converging on a geologically feasible model compared to other strategies that work with homogeneous or random starting models. The methodology's success stems from recognizing that starting models are not merely numerical conveniences but powerful tools for encoding geological understanding into mathematical optimization. Showing how appropriate initialization strategies can bridge the gap between geophysical data and geological reality, this work establishes a framework for developing more robust inversion algorithms applicable to complex geological environments where conventional approaches face problems of bodies without geological coherence and diffuse boundaries that are difficult to converge.

ACADEMIC DISSEMINATION

Conferences

- **Moreno-Sánchez, G.,** Goyes-Peñafiel, P., & Khurama-Velásquez, S. Inversión Gravitacional 3D con inicialización adaptativa y regularización secuencial: un estudio de caso en el área geotérmica de Cerro Machín. ***XX Congreso Colombiano de Geología***. Cali, Colombia. (2025, August 13-15).
- **Moreno-Sánchez, G.,** Goyes-Peñafiel, P., & Khurama-Velásquez, S. Modelamiento de anomalías gravimétricas 3D, caso de estudio: Volcán Cerro Machín. ***XVI Semana Técnica de Geología, Ingeniería Geológica y Geociencias***. Bucaramanga, Colombia. (2024, August 19-23).

ACKNOWLEDGMENT

This work was supported by the Agencia Nacional de Hidrocarburos and the Ministerio de Ciencia, Tecnología e Innovación under Project 110431 and CTO-045-2025.

REFERENCES

C. Alfaro, J. B. Rueda-Gutiérrez, Y. Casallas, G. Rodríguez, and J. Malo. Approach to the geothermal potential of Colombia. *Geothermics*, 96:102169, 11 2021. ISSN 0375-6505. doi: 10.1016/J.GEOTHERMICS.2021.102169. URL https://doi.org/10.1016/J.GEOTHERMICS.2021.102169.

Richard C Aster, Brian Borchers, and Clifford H Thurber. *Parameter estimation and inverse problems*. Elsevier, 2018. doi: 10.1016/C2009-0-61134-X. URL https://doi.org/10.1016/C2009-0-61134-X.

M.A. Beltrán. Gravimetría y magnetometría del área geotérmica del volcán Cerro Machín. Technical report, Servicio Geológico Colombiano, 2020.

T. N. Blaikie, L. Ailleres, P. G. Betts, and R. A.F. Cas. Interpreting subsurface volcanic structures using geologically constrained 3-D gravity inversions: Examples of maar-diatremes, Newer Volcanics Province, southeastern Australia. *Journal of Geophysical Research: Solid Earth*, 119:3857–3878, 2014. ISSN 21699356. doi: 10.1002/2013JB010751. URL https://doi.org/10.1002/2013JB010751.

Rowan Cockett, Seogi Kang, Lindsey J. Heagy, Adam Pidlisecky, and Douglas W. Oldenburg. SimPEG: An open source framework for simulation and gradient based parameter estimation in geophysical applications. *Computers and Geosciences*, 85:142–154, 12 2015. ISSN 00983004. doi: 10.1016/j.cageo.2015.09.015. URL https://doi.org/10.1016/j.cageo.2015.09.015.

Steven C Constable, Robert L Parker, and Catherine G Constable. Occam' s inversion: A practical algorithm for generatlng smooth models from electromagnetic sounding data. *GEOPHYSICS*, 52(3):289–300, 1987. doi: 10.1190/1.1442303. URL https://doi.org/10.1190/1.1442303.

Milton Burnett Dobrin and Carl H Savit. *Introduction to geophysical prospecting*. McGraw-hill. Fourth Edition, New York, 1960.

El Espectador. El volcán Cerro Machín, en Tolima, ha registrado un incremento en su actividad sísmica, 2024. URL https://www.elespectador.com/ambiente/el-volcan-cerro-machin-en-tolima-ha-registrado-un-incremento-en-su-actividad-sismica/.

Photograph retrieved from El Espectador, accessed on 2025-10-12. [In Spanish].

Colin G Farquharson and Douglas W Oldenburg. Nonlinear inversion using general measures of data misfit and model structure. *Geophys. J. Int*, 134:213–227, 2002. doi: 10.1046/j.1365-246x.1998.00555.x. URL https://doi.org/10.1046/j.1365-246x.1998.00555.x.

Colin G Farquharson, Michael R Ash, and Hugh G Miller. Geologically constrained gravity inversion for the Voisey's Bay ovoid deposit. *The Leading Edge*, 27 (1):64–69, 2008. doi: 10.1190/1.2831681. URL https://doi.org/10.1190/1.2831681.

J. S.Silva Dias Fernando, Valéria C.F. Barbosa, and João B.C. Silva. 3D gravity inversion incorporating prior information through an adaptive learning procedure. In *Society of Exploration Geophysicists - 77th SEG International Exposition and Annual Meeting, SEG 2007*, pages 745–749. Society of Exploration Geophysicists, 2007. ISBN 9781604238976. doi: 10.1190/sbgf2007-126. URL https://doi.org/10.1190/sbgf2007-126.

Clive A. Foss. Comparison of discrete and voxel 3-D gravity inversions over karst-related gravity anomalies on the coastal plain of north-west Malaysia. In *Proceedings of the Symposium on the Application of Geophyics to Engineering and Environmental Problems, SAGEEP*, volume 1, pages 544–553, 2005. ISBN 9781622760664. doi: 10.4133/1.2923499. URL https://doi.org/10.4133/1.2923499.

D Fournier and DW Oldenburg. Inversion using spatially variable mixed *ell*p norms. *academic.oup.com*, 218:268–282, 2019. doi: 10.1093/gji/ggz156. URL https://doi.org/10.1093/gji/ggz156.

Emad Ghalenoei, Jan Dettmer, Mohammed Y. Ali, and Jeong Woo Kim. Trans-dimensional gravity and magnetic joint inversion for 3-D earth models. *Geophysical Journal International*, 230:363–376, 7 2022. ISSN 1365246X. doi: 10.1093/gji/ggac083. URL https://doi.org/10.1093/gji/ggac083.

Antonio Guillen, Ph Calcagno, Gabriel Courrioux, Aurore Joly, and Patrick Ledru. Geological modelling from field data and geological knowledge: Part II. Modelling validation using gravity and magnetic data inversion. *Physics of the Earth and Planetary Interiors*, 171(1-4): 158–169, 2008. doi: 10.1016/j.pepi.2008.06.014. URL https://doi.org/10.1016/j.pepi.2008.06.014.

J. B. Rueda Gutiérrez. Reconocimiento geológico, estructural y modelo geológico 3D del área geotérmica del volcán Cerro Machín. Technical report, Servicio Geológico Colombiano, 2020.

Juan Herrera and Marco Calò. Geophysical characterization of the Cerro Machin geothermal area using three dimensional seismic and resistivity models. *Geothermics*, 131:103370, 9 2025. ISSN 0375-6505. doi: 10.1016/J.GEOTHERMICS.2025.103370. URL https://doi.org/10.1016/J.GEOTHERMICS.2025.103370.

Juan Camilo Herrera. Caracterización magnetotelúrica del área geotérmica de Cerro Machín. Technical report, Servicio Geológico Colombiano, 2020.

Philip Kearey, Michael Brooks, and Ian Hill. *An introduction to geophysical exploration*. John Wiley & Sons, 2013.

Peter G. Lelièvre and Douglas W. Oldenburg. A comprehensive study of including structural orientation information in geophysical inversions. *Geophysical Journal International*, 178:623–637, 8 2009. ISSN 0956540X. doi: 10.1111/J.1365-246X.2009.04188.X/2/M_178-2-623-EQ076.JPEG. URL https://dx.doi.org/10.1111/j.1365-246X.2009.04188.x.

Yaoguo Li and Douglas W. Oldenburg. 3-D inversion of magnetic data. *Geophysics*, 61:394–408, 1996. ISSN 00168033. doi: 10.1190/1.1443968. URL https://doi.org/10.1190/1.1443968.

Yaoguo Li and Douglas W. Oldenburg. 3-D inversion of gravity data. *Geophysics*, 63:109–119, 2 1998. ISSN 00168033. doi: 10.1190/1.1444302. URL https://doi.org/10.1190/1.1444302.

C. A. Miller, L. N. Schaefer, G. Kereszturi, and D. Fournier. Three-Dimensional Mapping of Mt. Ruapehu Volcano, New Zealand, From Aeromagnetic Data Inversion and Hyperspectral Imaging. *Journal of Geophysical Research: Solid Earth*, 125, 2 2020. ISSN 21699356. doi: 10.1029/2019JB018247. URL https://doi.org/10.1029/2019JB018247.

Craig A. Miller and Glyn Williams-Jones. Internal structure and volcanic hazard potential of Mt Tongariro, New Zealand, from 3D gravity and magnetic models. *Journal of Volcanology and Geothermal Research*, 319:12–28, 6 2016. ISSN 03770273. doi: 10.1016/j.jvolgeores.2016.03.012. URL https://doi.org/10.1016/j.jvolgeores.2016.03.012.

Craig A. Miller, Glyn Williams-Jones, Dominique Fournier, and Jeff Witter. 3D gravity inversion and thermodynamic modelling reveal properties of shallow silicic magma reservoir beneath Laguna del Maule, Chile. *Earth and Planetary Science Letters*, 459:14–27, 2 2017. ISSN 0012821X. doi: 10.1016/j.epsl.2016.11.007. URL https://doi.org/10.1016/j.epsl.2016.11.007.

Craig A. Miller, Jenny Barretto, Vaughan Stagpoole, Fabio Caratori-Tontini, Thomas Brakenrig, and Edward Bertrand. The integrated history of repeated caldera formation and infill at the Okataina Volcanic Centre: Insights from 3D gravity and magnetic models. *Journal of Volcanology and Geothermal Research*, 427, 7 2022. ISSN 03770273. doi: 10.1016/j.jvolgeores.2022.107555. URL https://doi.org/10.1016/j.jvolgeores.2022.107555.

Ethel Morales, Gerardo Veroslavsky, Alberto Manganelli, Josefina Marmisolle, Agostina Pedro, Lucía Samaniego, Facundo Plenc, Rodrigo Umpiérrez, Micaela Ferreiro, and Manuela Morales. Potential of geothermal energy in the onshore sedimentary basins of Uruguay. *Geothermics*, 95, 9 2021. ISSN 03756505. doi: 10.1016/j.geothermics.2021.102165. URL https://doi.org/10.1016/j.geothermics.2021.102165.

D. Mosquera, A. Núñez, and C. Vesga. Geología de la Plancha 244 – Ibagué. Mapa geológico a escala 1:100,000, 1982. Servicio Geológico Colombiano.

Wubamlak Nigussie, Abera Alemu, Kevin Mickus, Derek Keir, Zelalem Demissie, Yoseph Muhabaw, Ameha A. Muluneh, Giacomo Corti, and Esubalew Yehualaw. Subsurface structural control of geothermal resources in a magmatic rift: gravity and magnetic study of the Tulu Moye geothermal prospect, Main Ethiopian Rift. *Frontiers in Earth Science*, 11, 2023. ISSN 22966463. doi: 10.3389/feart.2023.1181533. URL https://doi.org/10.3389/feart.2023.1181533.

Douglas W. Oldenburg and Yaoguo Li. 5. inversion for applied geophysics: A tutorial. *Near-Surface Geophysics*, pages 89–150, 1 2005. doi: 10.1190/1.9781560801719.CH5. URL /doi/pdf/10.1190/1.9781560801719.ch5?download=true.

L. B. Pedersen and T. M. Rasmussen. The gradient tensor of potential field anomalies: some implications on data collection and data processing of maps. *Geophysics*, 55:1558–1566, 1990. ISSN 00168033. doi: 10.1190/1.1442807. URL https://doi.org/10.1190/1.1442807.

Nicolás Felipe Pedraza, Juan Diego Velásquez, Indira Molina, and Andrés Pedraza. Gravity Studies at the Cerro Machín volcano, Colombia. *Boletin Geologico*, 49:63–73, 2022. ISSN 27111318. doi: 10.32685/0120-1425/bol.geol.49.1.2022.619. URL https://doi.org/10.32685/0120-1425/bol.geol.49.1.2022.619.

Guomin Peng and Zhan Liu. 3D inversion of gravity data using reformulated Lp-norm model regularization. *Journal of Applied Geophysics*, 191, 8 2021. ISSN 09269851. doi: 10.1016/j.jappgeo.2021.104378. URL https://doi.org/10.1016/j.jappgeo.2021.104378.

Mahtab Rashidifard, Jérémie Giraud, Mark Lindsay, and Mark Jessell. Cooperative geophysical inversion integrated with 3-D geological modelling in the Boulia region, QLD. *Geophysical Journal International*, 238:860–880, 8 2024. ISSN 1365246X. doi: 10.1093/gji/ggae179. URL https://doi.org/10.1093/gji/ggae179.

Partha S. Routh, Leming Qu, Mrinal K. Sen, and Phil D. Anno. Inversion for non-smooth models with physical bounds. In *SEG Technical Program Expanded Abstracts*, volume 26, pages 1795–1799, 1 2007. doi: 10.1190/1.2792840. URL https://doi.org/10.1190/1.2792840.

Mauricio D Sacchi and Bin Liu. Minimum weighted norm wavefield reconstruction for AVA imaging. *Geophysical Prospecting*, 53(6):787–801, 2005. doi: 10.1111/j.1365-2478.2005.00503.x. URL https://doi.org/10.1111/j.1365-2478.2005.00503.x.

Jiajia Sun and Yaoguo Li. Adaptive Lp inversion for simultaneous recovery of both blocky and smooth features in a geophysical model. *Geophysical Journal International*, 197:882–899, 5 2014. ISSN 0956-540X. doi: 10.1093/GJI/GGU067. URL https://doi.org/10.1093/gji/ggu067.

Albert Tarantola. Inversion of seismic reflection data in the acoustic approximation. *Geophysics*, 49:1259–1266, 1984. ISSN 00168033. doi: 10.1190/1.1441754. URL https://doi.org/10.1190/1.1441754.

William Murray Telford, Lloyd P Geldart, and Robert E Sheriff. *Applied geophysics*. Cambridge university press, 1990.

Andrey N. Tikhonov and Vasiliy Y. Arsenin. *Solutions of Ill-Posed Problems*. Scripta Series in Mathematics. V. H. Winston & Sons, Washington, D.C.; New York: distributed solely by Halsted Press, 1977. ISBN 0470991240.

Sarah F. Trevino, Craig A. Miller, Basil Tikoff, Dominique Fournier, and Brad S. Singer. Multiple, Coeval Silicic Magma Storage Domains Beneath the Laguna Del Maule Volcanic Field Inferred From Gravity Investigations. *Journal of Geophysical Research: Solid Earth*, 126, 4 2021. ISSN 21699356. doi: 10.1029/2020JB020850. URL https://doi.org/10.1029/2020JB020850.

Leonardo Uieda and Valéria C.F. Barbosa. Use of the “shape-of-anomaly” data misfit in 3D inversion by planting anomalous densities. In *Society of Exploration Geophysicists International Exposition and 82nd Annual Meeting 2012, SEG 2012*, pages 867–872. Society of Exploration Geophysicists, 2012. ISBN 9781622769452. doi: 10.1190/segam2012-0383.1. URL https://doi.org/10.1190/segam2012-0383.1.

Chunlong Wei, Yanwu Guan, Xiaolong Li, Mingxing Sun, and Yangang Wu. Exploration of Shallow Geothermal Resources Based on Gravity and Magnetic 3D Inversion in the Wudalianchi–Laoheishan Volcano and Surrounding Areas. *Energies 2025, Vol. 18, Page 2011*, 18:2011, 4 2025. ISSN 1996-1073. doi: 10.3390/EN18082011. URL https://doi.org/10.3390/EN18082011.

Jeffrey B. Witter, Drew L. Siler, James E. Faulds, and Nicholas H. Hinz. 3D geophysical inversion modeling of gravity data to test the 3D geologic model of the Bradys geothermal area, Nevada, USA. *Geothermal Energy*, 4:1–21, 12 2016. ISSN 21959706. doi: 10.1186/S40517-016-0056-6. URL https://doi.org/10.1186/S40517-016-0056-6.

Xianzhe Yin, Changli Yao, Junlu Wang, Wenqiang Xu, Yuanman Zheng, Zelin Li, and Wenrui Mu. A constrained 3D gravity inversion for complex density distributions: Application to Brazil rifted continental margin. *Tectonophysics*, 874, 3 2024. ISSN 00401951. doi: 10.1016/j.tecto.2024.230236. URL https://doi.org/10.1016/j.tecto.2024.230236.

Dan Zhu, Xiangyun Hu, Shuang Liu, Hongzhu Cai, Shan Xu, Linghui Meng, and Henglei Zhang. Gravity inversion using L0 norm for sparse constraints. *Geophysical Journal International*, 236:904–923, 2 2024. ISSN 1365246X. doi: 10.1093/gji/ggad456. URL https://doi.org/10.1093/gji/ggad456.

APPENDIX A: GAUSS–NEWTON SOLUTION TO INVERSE PROBLEMS ADOPTING GENERAL MEASURES

If we use general measures of the length of vectors, the above objective function would become in equation (A1)). Therefore, the objective function to be minimized for the inverse problem considered in this paper has the following general form:

$$\Phi(\mathbf{m}) = \Phi_d^{(g)}\big[\,\mathbf{W}_d\big(\mathbf{d}^{\mathrm{obs}} - \mathbf{G}(\mathbf{m})\big)\big] + \beta \sum_{i=s,x,y,z} \alpha_i\, \Phi_i^{(g)}\big[\,\mathbf{W}_i \mathbf{m}\big]. \tag{A1}$$

Here, $\Phi_d^{(g)}$ is a symbolic representation of the data misfit defined by a general measure; similar notation is used for the model regularization terms.

Assume that at iteration $(k+1)$ we have the model $\mathbf{m}^{(k+1)}$ with predicted data $\mathbf{d}^{(k+1)} = \mathbf{G}(\mathbf{m}^{(k+1)})$. At the k-th iteration, we minimize the following objective in terms of the perturbation $\Delta\mathbf{m}$ to update the model (i.e. equation (9)):

$$\begin{aligned}\Phi(\Delta\mathbf{m}) = {} & \Phi_d^{(g)}\big[\,\mathbf{W}_d\big(\mathbf{d}^{\mathrm{obs}} - \mathbf{G}(\mathbf{m}^{(k+1)} + \Delta\mathbf{m})\big)\big] \\ & + \beta \sum_{i=s,x,y,z} \alpha_i\, \Phi_i^{(g)}\big[\,\mathbf{W}_i\big(\mathbf{m}^{(k+1)} + \Delta\mathbf{m}\big)\big].\end{aligned} \tag{A2}$$

The predicted data $\mathbf{d}^{(k)} = \mathbf{G}(\mathbf{m}^{(k)}) = \mathbf{G}(\mathbf{m}^{(k+1)} + \Delta\mathbf{m})$, at the kth iteration can be approximated by the first two terms in a Taylor expansion with respect to $\mathbf{m}^{(k+1)}$,

$$\mathbf{d}^{(k)} = \mathbf{d}^{(k+1)} + \mathbf{J}(\mathbf{m}^{(k)} - \mathbf{m}^{(k+1)}) = \mathbf{d}^{(k+1)} + \mathbf{J}\,\Delta\mathbf{m}, \tag{A3}$$

where $\mathbf{J}$ is the sensitivity (Jacobian) matrix with elements:

$$J_{ij} = \frac{\partial \mathbf{d}_i}{\partial \mathbf{m}_j}, \tag{A4}$$

we can rewrite equation (A2) as

$$\begin{aligned}\Phi(\Delta\mathbf{m}) = {} & \Phi_d^{(g)}\big[\,\mathbf{W}_d\big(\mathbf{d}^{\mathrm{obs}} - \mathbf{d}^{(k+1)} - \mathbf{J}\,\Delta\mathbf{m}\big)\big] \\ & + \beta \sum_{i=s,x,y,z} \alpha_i\, \Phi_i^{(g)}\big[\,\mathbf{W}_i\big(\mathbf{m}^{(k+1)} + \Delta\mathbf{m}\big)\big].\end{aligned} \tag{A5}$$

We next consider the differentiation of the general measures given in equation (A5) with respect to $\Delta\mathbf{m}$. For convenience, we reformulate equation (A5) as follows:

$$\Phi(\Delta\mathbf{m}) = \Phi_d^{g}(\mathbf{X}_d) + \beta \sum_{i=s,x,y,z} \alpha_i\, \Phi_i^{g}(\mathbf{X}_i)\,, \tag{A6}$$

where

$$\mathbf{X}_d = \mathbf{W}_d\big(\mathbf{d}^{\mathrm{obs}} - \mathbf{d}^{(k+1)} - \mathbf{J}\,\Delta\mathbf{m}\big), \tag{A7}$$

$$\mathbf{X}_i = \mathbf{W}_i\big(\mathbf{m}^{(k+1)} + \Delta\mathbf{m}\big). \tag{A8}$$

We apply the chain rule for vector functions. The derivative of $\Phi(\Delta\mathbf{m})$ with respect to $\Delta\mathbf{m}$ is given by

$$\frac{\partial \Phi}{\partial(\Delta\mathbf{m})} = \frac{\partial \mathbf{X}_d}{\partial(\Delta\mathbf{m})}\,\frac{\partial \Phi_d^{(g)}}{\partial \mathbf{X}_d} + \beta \sum_{i=s,x,y,z} \alpha_i\, \frac{\partial \mathbf{X}_i}{\partial(\Delta\mathbf{m})}\,\frac{\partial \Phi_i^{(g)}}{\partial \mathbf{X}_i}. \tag{A9}$$

From equation (A7) and (A8) we have

$$\frac{\partial \mathbf{X}_d}{\partial(\Delta\mathbf{m})} = -\,\mathbf{J}^{\top}\mathbf{W}_d^{\top}, \tag{A10}$$

$$\frac{\partial \mathbf{X}_i}{\partial(\Delta\mathbf{m})} = \mathbf{W}_i^{\top}. \tag{A11}$$

Inserting equation (A10) and equation (A11) into equation (A9) yields the following equation:

$$\frac{\partial \Phi}{\partial(\Delta\mathbf{m})} = -\,\mathbf{J}^{\top}\mathbf{W}_d^{\top}\,\frac{\partial \Phi_d^{(g)}}{\partial \mathbf{X}_d} + \beta \sum_{i=s,x,y,z} \alpha_i\, \mathbf{W}_i^{\top}\,\frac{\partial \Phi_i^{(g)}}{\partial \mathbf{X}_i}. \tag{A12}$$

For the Ekblom norm used in this study,

$$\Phi_d^{(g)}(\mathbf{X}_d) = \sum_{k=1}^{n} \big(X_{dk}^2 + \varepsilon^2\big)^{p/2}, \tag{A13}$$

which gives

$$\frac{\partial \Phi_d^{(g)}}{\partial X_{dk}} = p\, X_{dk}\big(X_{dk}^2 + \varepsilon^2\big)^{\frac{p}{2}-1}. \tag{A14}$$

Hence, in vector form

$$\frac{\partial \Phi_d^{(g)}}{\partial \mathbf{X}_d} = \mathbf{R}_d\,\mathbf{X}_d, \tag{A15}$$

$$\mathbf{R}_d = \mathrm{diag}\Big(p\big(X_{d1}^2 + \varepsilon^2\big)^{\frac{p}{2}-1}, \ldots, p\big(X_{dn}^2 + \varepsilon^2\big)^{\frac{p}{2}-1}\Big). \tag{A16}$$

By the same reasoning,

$$\frac{\partial \Phi_i^{(g)}}{\partial \mathbf{X}_i} = \mathbf{R}_i\,\mathbf{X}_i, \qquad i = s, x, y, z, \tag{A17}$$

with $\mathbf{R}_i$ defined analogously.

$$\frac{\partial \Phi(\Delta \mathbf{m})}{\partial \Delta \mathbf{m}} = -\mathbf{J}^\top \mathbf{W}_d^\top \mathbf{R}_d \mathbf{X}_d + \beta \sum_{i=s,x,y,z} \alpha_i \mathbf{W}_i^\top \mathbf{R}_i \mathbf{X}_i. \tag{A18}$$

Substituting (A7)–(A8), (A15), (A16) and (A17) into (A12) yields

$$\begin{aligned}\frac{\partial \Phi}{\partial (\Delta \mathbf{m})} =& -\mathbf{J}^\top \mathbf{W}_d^\top \mathbf{R}_d \mathbf{W}_d \big(\mathbf{d}^{\text{obs}} - \mathbf{d}^{(k+1)} - \mathbf{J}\,\Delta \mathbf{m}\big) \\ & + \beta \sum_{i=s,x,y,z} \alpha_i \mathbf{W}_i^\top \mathbf{R}_i \mathbf{W}_i \big(\mathbf{m}^{(k+1)} + \Delta \mathbf{m}\big).\end{aligned} \tag{A19}$$

Setting the gradient to zero leads to the linear system to be solved at iteration n:

$$\begin{aligned}&\left[\mathbf{J}^\top \mathbf{W}_d^\top \mathbf{R}_d \mathbf{W}_d \mathbf{J} + \beta \sum_{i=s,x,y,z} \alpha_i \mathbf{W}_i^\top \mathbf{R}_i \mathbf{W}_i\right] \Delta \mathbf{m} \\ &= \mathbf{J}^\top \mathbf{W}_d^\top \mathbf{R}_d \mathbf{W}_d \big(\mathbf{d}^{\text{obs}} - \mathbf{d}^{(k+1)}\big) \\ &\quad - \beta \sum_{i=s,x,y,z} \alpha_i \mathbf{W}_i^\top \mathbf{R}_i \mathbf{W}_i \big(\mathbf{m}^{(k+1)}\big),\end{aligned} \tag{A20}$$

This system is readily solved with a conjugate-gradient method to obtain $\Delta \mathbf{m}$ and update the model. At each iteration, matrices $\mathbf{R}_i$ $(i = d, s, x, y, z)$ and the Jacobian $\mathbf{J}$ are recomputed from the updated model $\mathbf{m}^{(k)}$. The procedure is the standard iteratively reweighted least squares (IRLS) scheme for non-linear inverse problems.

APPENDIX B: NOMENCLATURE OF THE ℓ_p NORM

In this appendix, we use generalized ℓ_p regularization to simultaneously control the smallness of the model and its directional roughness. The total cost is

$$\Phi(\mathbf{m}) \;=\; \Phi_d(\mathbf{m}) \;+\; \beta\,\Phi_m(\mathbf{m}), \tag{B1}$$

where Φ_d is the data misfit (dimensionless chi-square) and Φ_m is the model objective function. The latter consists of two parameters, Φ_{small}, which penalizes how large the model is relative to a reference model ($\mathbf{m}_{ref}$) or, in this case, relative to zero, while Φ_{smooth} is the sum of the derivative terms (x, y, z) and penalizes the spatial roughness of the model to make it smoother.

$$\Phi_m = \Phi_{small} + \Phi_{smooth}. \tag{B1}$$

In a more developed form, we find it as:

$$\begin{aligned}\Phi_m = \alpha_s & \int_v \mathbf{w}_s \,|\mathbf{m}|^{p_s}\, dv \\ & + \alpha_x \int_v \mathbf{w}_x \left|\frac{\partial \mathbf{m}}{\partial x}\right|^{p_x} dv + \alpha_y \int_v \mathbf{w}_y \left|\frac{\partial \mathbf{m}}{\partial y}\right|^{p_y} dv \\ & + \alpha_z \int_v \mathbf{w}_z \left|\frac{\partial \mathbf{m}}{\partial z}\right|^{p_z} dv.\end{aligned} \tag{B2}$$

The choice of p∈[0,2] governs the morphology of the solution:

- $p = 2$: quadratic penalty (Tikhonov), smooth and continuous models;
- $p = 1$: L_1 penalty, blocked models with sharp edges;
- $p \to 0$: *focusing* (maximum compactness), useful for discrete bodies.